Silver quasi-nanoparticles: bridging the gap between clusters molecular-like and plasmonic nanoparticles

Fatima Douma, Louwanda Lakiss, Oleg I Lebedev, Julien Cardin, Krassimir L Kostov, Jaafar El Fallah, Valentin Valtchev, Mohamad El-Roz

ARTICLE

Silver quasi-nanoparticles: bridging the gap between clusters molecular-like and plasmonic nanoparticles

Received 00th January 20xx,
Accepted 00th January 20xx

DOI: 10.1039/x0xx00000x

Fatima Douma[a], Louwanda lakiss[a], Oleg I. Lebedev[b], Julien Cardin[c], Krassimir L. Kostov[d], Jaafar El Fallah[a], Valentin Valtchev[a] and Mohamad El-Roz[a]*

Herein, we report a new strategy for preparing connected silver sub-nanoparticles with unique optical behavior via a selective photo-assisted electrochemical reduction of silver cations in FAU-type zeolite X (FAUX) cages. Bi^{2+}/Bi^{3+} doped zeolite nanoparticles (ZX-Bi) were prepared by one-pot hydrothermal synthesis and stabilized as colloidal water suspension. Silver nitrate-containing ZX-Bi suspension was subjected to UV irradiation resulting in the reduction of silver cations and generation of $Ag^{\&+}_n$ clusters (Ag@ZX-Bi). The physicochemical characterization of the samples, using XRD, TG, N2 sorption, NMR, HRTEM-STEM, ICP, EDX and XPS analyses, provided comprehensive information on the textural and structural properties, the chemical compositions and the metal oxidation state of the samples. Their optical behaviors have been investigated using UV-visible and photoluminescence spectroscopies. The IR-operando analysis under visible-light revealed local heating of Ag@ZX-Bi up to 400K. The theoretical calculation of the absorption, scattering, and extinction cross-sections σ_{abs}, σ_{sca} and σ_{ext} of different silver models performed in this study, was in agreement with the experimental data, elucidating the unique optical behavior of the silver particles. The set of analyses show that quasi-nanoparticles of Ag are formed from bridged Ag clusters (AgCLs) through zeolite channels closing for the first time the gap between clusters and plasmonic nanoparticles.

1 Introduction

The Downsizing the dimension of metallic particles to the nanometer, sub-nanometer and quasi-atomic level provides a new ground for achieving novel structural, electronic and optical properties. One of the consequences of reducing the size of the metallic particles to less than the Fermi wavelength is their molecular-like behavior with intralevel energy exceeding the thermal activation energy (K_BT), which gives rise to size-dependent HOMO-LUMO band gap comparable with that of semiconductors. Thus, the layer-dependent transitions of silver clusters render them optically active emissive centers[1,2]. However, the interaction between the incident light, at a specific wavelength, and metal nanoparticles (MNPs) could induce collective oscillations of the conduction electrons, producing a Local Surface Plasmonic Resonance (LSPR) with no direct luminescence properties[3]. These behaviors make them very attractive for various applications in solar-cell[4], imaging[5], biomedecine[6-8], (bio)sensing[9,10], etc.

Several recent research studies aimed to prepare M-NPs and metal clusters (M-CLs) with ordered shape and size.[1-10] They focused on tuning the metal clusters physicochemical properties (size, morphology, charge) to improve their performance. The crucial key to reaching this objective is to control the metal atoms' self-assembling processes and stabilize their nucleation at a well distinct stage.

In the case of M-CLs, one of the main challenges is their stability, as they are susceptible to agglomerate into larger particles due to their high surface energy. Typically, organic stabilizing agents (micelles formation with M-NPs core) or porous host support are used to ensure their stability[11,12]. Several recent works show that the use of zeolite as a host environment is one of the most convenient strategies for promoting the formation of well-defined M-CLs. For instance, embedding few silver atoms and clusters in the well-defined dielectric cavities of zeolite reveals novel optical properties with respect to the plasmonic silver nanoparticles (Ag-NPs). This behavior is dependent on multiple factors, including the size, geometry, degree of hydration, and the electrostatic interaction between the metal and the local host environment[13,14].

The silver clusters (Ag-CLs) in the zeolite pores are usually prepared by thermal treatment of zeolite exchanged with silver cations at a relatively high temperature (>450°C). The final materials' optical properties strongly depend on the framework topology and charge density of the zeolite, its counter-ions, the degree of silver exchange, and their hydration states[15,16]. However, a very low concentration of silver is required in order to minimize the migration of the silver

[a] Normandie Université, ENSICAEN, UNICAEN, CNRS, Laboratoire Catalyse et Spectrochimie, 14050 Caen, France.
[b] Laboratoire CRISMAT, ENSICAEN, CNRS UMR 6508, 14050 Caen, France.
[c] Laboratoire CIMAP, Normandie Université, ENSICAEN, UNICAEN, CNRS UMR6252, CEA, 14000 Caen, France.
[d] Bulgarian Academy of Sciences, Institute of General and Inorganic Chemistry,1113 Sofia, Bulgaria.

* E-mail address: mohamad.elroz@ensicaen.fr
Electronic Supplementary Information (ESI) available: [details of any supplementary information available should be included here]. See DOI: 10.1039/x0xx00000x

clusters and their agglomeration into large particles. Therefore, only a few isolated clusters can be obtained with interesting emission behavior in visible light.

Recently, we demonstrated that Ag-CLs can be prepared under soft irradiation conditions at RT[17]. We showed that a UV irradiation of a suspension of faujasite X (FAUX) doped with vanadium oxide clusters (ZX-V), promotes a local reduction of silver nitrate into Ag-CLs, via a photocatalytic-like process in the presence of ethanol as an electron donor. Due to the limited loading of the highly dispersed vanadium oxide clusters in the zeolite, only isolated Ag-CLs and some external Ag-NPs were obtained.

Herein, we report an innovative and selective strategy for preparing Ag-CLs in FAUX doped with Bi^{2+}/Bi^{3+} cations via a local photoassisted electrochemical reduction of Ag cations. The successful preparation of highly crystalline zeolite with abundant Bi active sites and the localization of these later in sodalite and double six-membered ring (6MR) prism offered a unique opportunity for bridging the reduced silver clusters through the zeolite channel instead of isolated clusters obtained previously. Contrary to our previous photocatalytic process, the new process is a photo-assisted electrochemical approach that can be even performed in dark. With the new approach, the optical behaviors of Ag-CLs can be easily tuned by adjusting the amount of Bi without changing the host environment.

2 Experimental

Materials: The following chemical products were purchased and used without further purification: Al powder (325 mesh, 99.5 %, Alfa Aesar), NaOH (VWR Chemicals-Prolabo, 99 %), SiO_2 (Ludox-AS 30, 30 wt. % SiO_2, pH=9.8, Aldrich), $Bi(NO_3)_3.5H_2O$ (99.9%, Aldrich), $Ag(NO_3)$ (99.9%, Aldrich).

The Ag@ZX-Bi sample was prepared using the synthesis procedure that was previously reported in our recent work for the preparation of Ag@ZX-V [**Error! Bookmark not defined.**]. First ZX-Bi is prepared by in situ incorporation of bismuth as a metal precursor for photoactive species in the synthesis mixtures:

Synthesis of ZX-Bi: As a first step, the nanosized ZX-Bi-x samples were synthesized according to sol-gel method without employing an organic template (x: represents the weight percentage, which varies between 0.5 and 10 wt.%, relative to the weight of alumina and silica). In a typical synthetic procedure, sodium aluminate and sodium silicate are prepared separately (denoted solutions A and B, respectively). The sodium aluminate was prepared by adding 0.5 g of sodium hydroxide to 3 g of water in a plastic bottle. Then the aluminum powder was slowly dispersed under vigorous stirring until this latter is completely dissolved. After that bismuth (III) nitrate pentahydrate ($Bi(NO_3)_3.5H_2O$) was introduced into the solution and was sonicated for 30 min to completely dissolve the $Bi(NO_3)_3$. Sodium silicate is prepared concurrently by adding 1 g of NaOH to 1 g of water and 10 g of colloidal silica suspension at room temperature. The obtained sol was heated for 7 min at 90°C until a clear sol was formed and kept under stirring. Solution A was added dropwise into the solution B under intensive stirring after placing this later in an ice bath in order to control the exothermicity of the reaction. The formed sol-gel mixture was aged for 14h to 24h at room temperature. The water content was adjusted using a freeze dryer to avoid aggregation. The solution was then crystallized at 50° C for 24h. The molar composition of the clear gel is given as: 10 SiO_2: 1.1 Al_2O_3: x Bi: 9 Na_2O: 122H_2O (x = 0.066, 0.20, 0.40, 0,66 atm.% equivalent to 0.5, 1.5, 3.0 and 5.0 wt.% of Bi in respect to (Si+Al), respectively). Then, very stable suspensions were obtained. The solid was recovered by centrifugation (25 min, 20000 rpm) followed by re-dispersion in double-distilled water. The procedure was repeated until reaching pH~8. It has been observed that the crystallinity and the purity of ZX-Bi are strongly affected by the amount of bismuth precursor added to the initial synthesis mixture. In order to obtain a high crystalline and pure ZX-Bi sample, the synthesis parameters such as the aging and crystallization times, the amount of water eliminated by freeze-drying and the Bi content have been optimized. The optimization processes and the results are detailed in the supplementary information. To estimate the crystallinity of zeolite samples, a Bi-free highly ZX sample is used as reference. Then the crystallinity of the as-synthesized samples was estimated by comparing the integrated area of the reflection peaks of ZX-Bi relatively to their corresponding peaks in the pure ZX.

Preparation of Ag@ZX-Bi: Zeolite samples with different content of Bi are prepared to investigate the effect of Bi content on the evolution of silver species formation. Ag@ZX-Bi samples were prepared by dispersing ZX-Bi (2.4g/l) in pure water or in water solutions containing ethanol and silver nitrate (10 mM) with a ratio of ethanol/water=1/3. Upon UV irradiation (Hg-Xe lamp; polychromatic irradiance = 205 mW/cm^2; infrared cut filter), the color of the suspension changes from white to pinke, confirming the reduction of silver Ag_n^{n+} to $Ag_n^{\delta+}$ clusters (with $\delta<n$). The optical penetration depth of zeolite-based structures has been evaluated leading to determine that UV radiations are transmitted at least partially through the walls of these structures. Thanks to the known refractive indexes of the zeolite material's constituent (H_2O, SiO_2, Al_2O_3), we estimate that the optical penetration depth, defined as the depth at which the intensity of the radiation inside the material, falls to 1/e at different UV wavelengths ranging from 240 to 365 nm. Penetration depths were found to range from 7.8 nm in pure Al_2O_3 to 6 meters in pure water at 365nm. These extreme values frame the depth of penetration into the walls of zeolite-based structures. In view of the dimensions of the zeolite-based structures, it can therefore be concluded that the UV radiation is transmitted at least partially through the walls of these structures. In addition, the concentration of the zeolite suspension (2mg/ml) as well as the optical pathway (10-20 cm) was optimized (based on our previous study) in order to obtain a very reproducible results (many grams of Ag@ZXBi-3 was prepared and correspond to a treatment of 10's of samples).

Characterization techniques: UV–vis spectroscopy measurements were performed using a Cary 4000 UV–Vis spectrophotometer at room temperature in transmission mode using a quartz cuvette with a 1 cm path length. The absorbance spectra were corrected by subtracting the spectrum of pure zeolite (ZX). The DR-UV-Vis spectra of the dried powder samples were recorded using RSA-CU40 Diffuse Reflectance cell. The spectrum of the non-irradiated sample was subtracted from the spectra of irradiated samples. The chemical composition of the samples was measured on a Varian Vista AX CCD inductively coupled plasma atomic emission spectrometer (ICP-AES). The continuous wave (CW) photoluminescence (PL) measurements were carried out at room temperature using two excitation lasers: a Crylas FQCW266 emitting at 266 nm with an average power of 27 mW, and a coherent Innova 90C argon laser with an average power of 150mW at 488nm. The excitation was done with an incident angle of 45° on a beam spot size of about 1 mm² and chopped at 3.00 Hz for samples. Emitted photons were collected by means of a set of lenses until a Horiba Jobin-Yvon Triax 180 monochromator. At the exit of this monochromator, a R5108 Hamamatsu photomultiplier tube ensures photon detection. This detected signal is amplified by means of a Femto DLPCA-200 trans-impedance amplifier and send to a SR830 lock-in amplifier referenced at the excitation laser chopper frequency. Different High pass filter cutting at 500 nm or 700 nm were used respectively to prevent the collection of excitation line by the detection system and prevent eventual second-order contributions. PL spectra were measured on sample powder stacked between two quartz Suprasil(TM) glass slides from Hellma Analytics. The water content and stability of the samples were investigated by Thermogravimetric analysis (TGA) using a SETSYS instrument (SETARAM) analyzer (heating rate of 5 °C min^{-1} under 40 $ml.min^{-1}$ flow of air).

The structural and morphological features of the samples were investigated with a transmission electron microscopy (TEM) using an aberration probe and image corrected JEM ARM200F cold FEG microscope operated at 200 kV equipped with a CENTURIO EDX detector and GIF Quantum spectrometer. Specimens for transmission electron microscopy studies were dispersed in ethanol and drop cast onto a Cu holey carbon grid.

The crystallinity and phase purity of zeolite samples were studied by powder X-ray diffraction analysis (PXRD) using a PANalyticalX'Pert Pro diffractometer with CuKα-moy wavelength (λ = 1.5418 Å). The PXRD diagrams were recorded at room temperature between 3 and 50° (2θ) with a step size of ~0.014°(2θ). Variable divergent slits with a constant illuminated sample length of 6 mm were used. Phase identification was performed with a PANalyticalHighScore plus program. Nitrogen sorption analyses were performed on a Model ASAP 2020 apparatus. After degassing at 200 °C under vacuum for 12 h, the samples were then cooled, and nitrogen adsorption is performed. Specific surface areas were determined from BET equation. The total pore volume is the total volume adsorbed at P/P°=0.99. The *t*-plot method was used to distinguish the micropores from the mesopores in the samples. The pore size distribution (PSD) was derived from the desorption branch of the N_2 isotherm using the Barrett-Joyner-Halenda (BJH) algorithm.

Aluminum MAS NMR experiments were performed on a 500 MHz Bruker AVANCE III spectrometer operating at 130.32 MHz for ^{27}Al, and equipped with a double resonance 4 mm probe head.

X-ray photoelectron spectroscopy (XPS) measurements were carried out on an AXIS Supra electron spectrometer (Kratos Analyical Ltd.) with base vacuum in the analysis chamber in the order of 10^{-8} Pa. The samples are irradiated with monochromatized Al Kα radiation with photon energy of 1486.6 eV. The photoemitted electrons were separated, according to their kinetic energy, by 180° - hemispherical analyzer with a total instrumental resolution of 0.6 eV (as measured by the FWHM of Ag 3d5/2 line) at pass energy of 20 eV. Due to charging effect, a resolution of ≈1.0 eV has been measured on the selected samples. Energy calibration was performed by normalizing the C 1s line of adventitious adsorbed hydrocarbons on silver folio 284.6 eV. The diameter of the analysis area was 700x300 μ^2.

Operando IR experiments was performed using 'sandwich like' IR cell-reactor[18]. The FITR spectra of the samples (shaped as a pellet of ~ 20 mg with 65 µm of thickness) were recorded under Ar and at different temperatures. The employed ThermoNicolet NEXUS 670 FTIR was equipped with an MCT detector with a spectral resolution of 4 cm^{-1} and time resolution of 1 spectrum/s. The irradiation of the samples with visible light was performed using a Xe-lamp (LC8 Hamamatsu, 200 W) equipped with a cut-UV filter (λ>390nm).

For CO-adsorption, the sample, activated in an in-situ IR cell, was first cooled to -173°C under vacuum. Then, small doses of 0.5-10 µmol of CO were introduced to the cell. IR spectra were recorded after each dose. IR spectra were recorded with a Nicolet Magna 550-FT-IR spectrometer at 4 cm^{-1} optical resolution. Prior to the measurements, the samples were pressed into self-supporting discs (diameter: 1.6 cm, 20 mg) and pretreated in the IR cell attached to a vacuum line (10^{-6} Torr), at 100°C for 18 h.

The boundary element method (*BEM*) approach presented by F. J. Garcia de Abajo et al.[19] and developed by U. Hohenester et al.[20] in *MNPBEM* MatLab toolbox was used in order to model the far-field response of singular silver objects. The silver nanostructures models were built based on the TEM data, which help to localize and determine particle sizes of Ag clusters. Then, the absorption, scattering, and extinction cross-sections σ_{abs}, $\sigma_{\sigma ca,}$ and σ_{ext} of the structure models have been calculated. The silver nanostructures in Faujasite structure are reproduced by the alternation of large diameter spherical silver nanoparticles (LNp; 1.1 nm) for the sodalite cages and small diameter (SNp; 0.7 nm) for the hexagonal prisms. The effect of Nps interconnection was investigated by comparing the response of silver nanostructure with isolated and interconnected nanoparticles. Silver nanostructures were also simulated with the increasing number of Faujasite unit cells of 1, 2, 5 and 10 to reproduce the different structures with various lengths observed by TEM. The surrounding medium was considered as water with constant permittivity (ε=1.332) and silver permittivity was taken from reference [21]. It should be underlined that the simulations simplify our experimental system. For example, the global charge of the clusters, the presence of Bi^{3+}, the zeolite-Ag interaction, and the silver Nps size may change the silver permittivity with respect to the one of bulk silver in the standard. Moreover, supplementary

orientation effects and overlapping of many objects (silver nanostructures) may complicate the plasmon response. Although this simulation will not give a response strictly identical to that observed in complex experimental systems, its contribution is representative and significant for the interpretation.

3 Results and discussion

Highly crystalline ZX-Bi samples were obtained after an extensive optimization of the synthesis parameters. It should be noted that ZX-V is used in this work as a reference. Details about the ZX-V sample can be found in ref. 17 and the supporting information. The XRD results demonstrate that the presence of Bi in the synthesis media significantly affects the crystal growth kinetics of zeolite X (**Fig. 1** and Figures S1-S3). We attribute this effect to the additional charge. Thus, the presence of bismuth reduces the crystallization time from 24h to 8 h, compared to the Bi-free sample (ZX) prepared under similar synthesis conditions. The maximal amount of bismuth introduced in the synthesis media without perturbing the crystallization processes is 3.0 wt.% (in respect to the Si and Al amounts) (**Fig. 1**). For simplification, the "x" values in the ZX-Bi-x samples correspond to the amount of Bi initially introduced. For a higher bismuth concentration (> 5 wt.% Bi), the crystallization of Faujasite is altered, and sodalite arises as the major crystalline product (Table S1; Figure S1-S3). Thus, at larger amounts the Bi perturbs the structure directing role of Na^+ and consequently the final zeolite product.[22] The XRD pattern of ZX-Bi-3 didn't show any evidence of the presence of crystalline Bi oxide (**Fig. 1**). The broadening of the XRD peaks is due to the nanosized dimensions of zeolite particles as shown by the DLS analysis. The hydrodynamic diameters of ZX and ZX-Bi particles is 45 and 50 nm, respectively (Figure S4). Hence, ZX-Bi shows similar crystallinity of the parent zeolite ZX with no extra-framework alumina detected (Figure S5), when it is prepared under the optimal conditions cited above.

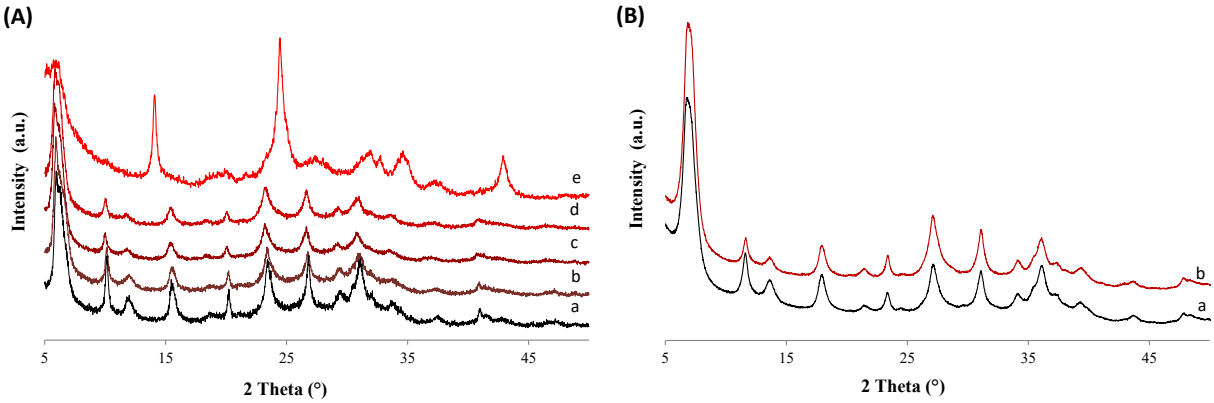

Fig. 1. (A) X-ray diffraction patterns of ZX-Bi samples prepared with different bismuth contents: (a) 0 wt.% (ZX or ZX-Bi-0), (b) 0.5 wt.% (ZX-Bi-0.5); 1.5 wt.% (ZX-Bi-1.5), (c) 3.0 wt.% (ZX -Bi-3), and (d) 5.0 wt.% (ZX-Bi-5). Samples crystallized at 50 °C for 8 h after aging for 14h at RT. The weight percentage of bismuth corresponds to the initial quantities added and calculated by considering the quantity of Al and Si. (B) XRD patterns of (a) pure ZX and (b) ZX-Bi-3 crystallized for 24 h and 8 h, respectively. Crystallization temperature: 50 °C; after aging for 24 h and 14 h at RT, respectively.

According to the ICP analysis, the bismuth amounts in ZX-Bi-0.5, ZX-Bi-1.5 and ZX-Bi-3 samples are 0.38, 1.15 and 2.3 wt.%, respectively (equivalent to 0.18, 0.33 and 0.74 atm. %). The Si/Al ratio was in the range of 1.3 to 1.5 in all samples, in agreement with the EDX results (Table S2). The loss of the Bi during the synthesis is relatively low (around 25%) in respect to that previously observed when vanadium precursor was used (around 90%)[17]. This is probably due to the counter-ion role that Bi^{n+} plays for compensating the negative charge of oxygen lattice.

The textural properties of the ZX-Bi-3 compared with the reference ZX sample are assembled in **Fig. 2.** The N_2 adsorption data analysis of ZX and ZX-Bi-3 sample (**Fig. 2A**) shows a combination of I and IV type isotherms with a large hysteresis H1 type loop. The latter corresponds to a material with textural porosity originating from packed uniform in size nanoparticles[23]. The slightly lower micropore volume of ZX-Bi compared to pure ZX (**Fig. 2B**) might be due to a slightly lower crystallinity of the sample (95% in respect to the pure ZX). It should be noted that the pore size distribution for ZX and ZX-Bi-3 (**Fig. 2B**) in the mesopore range is identical pointing out a similar particle size and regular textural porosity. The thermal analysis of ZX sample (**Fig. 2C**) shows water weight loss with two endothermic peaks at around 80°C and 140°C that correspond to the dehydration of physiosorbed and structural water, respectively. However, the elimination of water in the ZX-Bi sample takes place at a relatively higher temperature (125°C and 200°C). This could be related to the higher water affinity of multivalent Bi cations.

The electron microscopy study (**Fig. 3** and Figure S6) confirmed the presence of highly dispersed Bi in the zeolite. It is challenging to localize the Bi particle with precision in the zeolite structure base on the TEM analysis, which is due to their low concentration and high mobility under the electron-beam. In this respect, the HAADF-STEM is considered a more appropriate technique due to the atomic

number dependence (~ Z^2) and sensitivity to a small amount of material (down to single atoms). The HAADF-STM images reveal the presence of ordered Bi atoms along the [112] plane (**Fig. 3a**), which are mainly located in the sodalite cage and double six-member ring (6MR) prism (Figure 3b-d).

Ag@ZX-Bi-3 samples were prepared by UV irradiation of the ZX-Bi-3 suspensions in the presence of $AgNO_3$. Then the samples were washed with deionized water three times in order to remove the non-reacted silver nitrate. The XPS analysis performed on ZX-Bi-3 and Ag@ZX-Bi-3 samples shed more light on the Bi's nature before and after Ag^+ reduction. In the case of the parent sample (ZX-Bi), in addition to the main signal observed at 153.3 eV and attributed to silicon (Si 2s). The high-resolution XPS spectra (**Fig. 4**) shows characteristic peaks of Bi^{3+} and Bi^{2+}: 1) the Bi 4f core level spectrum with two spin-orbit doublet peaks (J=5/2 and 7/2) centered at 165 (Bi 4f5/2) and 159.5 eV (Bi 4f7/2) with a peak separation of 5.5 eV, and 2) the pair of peaks at lower binding energies 163 and 157.3 eV with a peak separation of 5.7 eV, respectively[24-26]

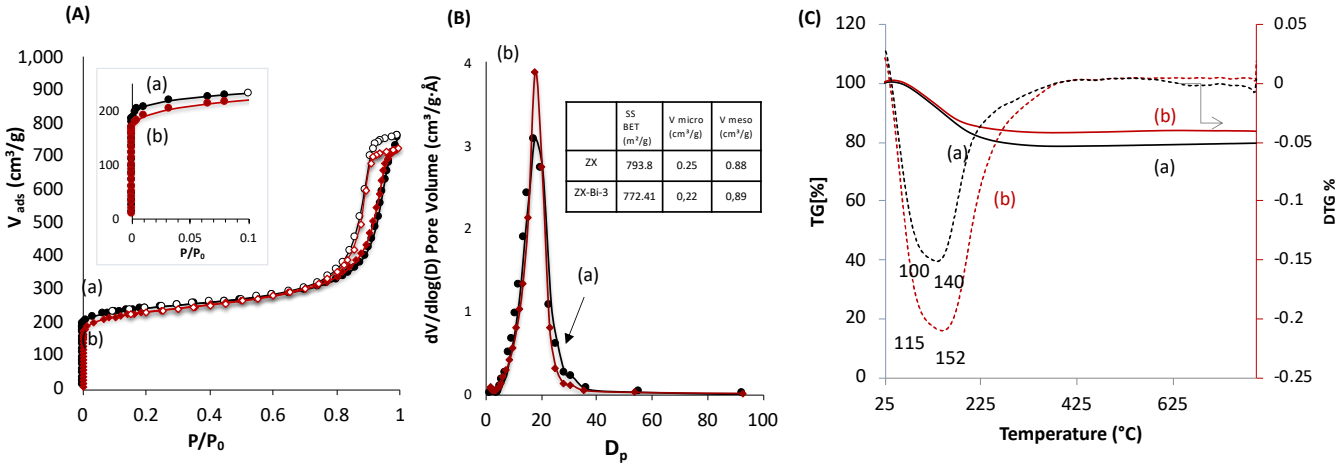

Fig.2. (A) Nitrogen adsorption and desorption isotherms, (B) mesopore size distribution, and (C) TG (solid lines) and DTG (doted lines) curves of (a) ZX and (b) ZX-Bi-3 samples.

The chemical composition obtained with XPS is very close to that obtained by ICP and EDX analyses, confirming the homogeneous distribution of Bismuth cations. The unexpected detection of Bi^{2+} in ZX-Bi-3 sample reveals a chemical reduction of Bi^{3+} precursor during the synthesis process. The reduction of Bi^{3+} to its lower-valence bismuth ions usually occurs after thermal treatment at a relatively high temperature under anaerobic atmosphere conditions[27]. The low synthesis temperature (50°C) excludes the thermal reduction hypothesis, which is probably due to the in in-situ loading of Bi in presence of metallic alumina in the synthesis, characterized with a very low standard potential (-1.67 V SHE, for Al^{3+}/Al at 25°C) in respect to Bi^{3+}/Bi (+0.317V SHE at 25°C). The XPS analysis shows that Bi^{2+} and Bi^{3+}coexisted with Bi^{2+}/Bi^{3+} ratio of 2.3. This result was confirmed on two different ZX-Bi-3 samples (with an error of below 10 %). We anticipate two different positions of Bi^{2+} and Bi^{3+} counter cations compensating the $(AlOSi)^-$ charges of zeolite framework; Sun *et al.*[28] demonstrated by high-resolution synchrotron XRD analysis of dehydrated zeolite that Bi^+ with an ionic radius of 1.45 Å occupies single-type site I' in the sodalite cage of FAU-type zeolite, where it is coordinated with three oxygen atoms of the 6MR prism. However, the characteristic ionic radius of Bi^{2+} and Bi^{3+} are 1.16 and 0.96 Å (*vs* 1.0 Å for Na^+), respectively[28].

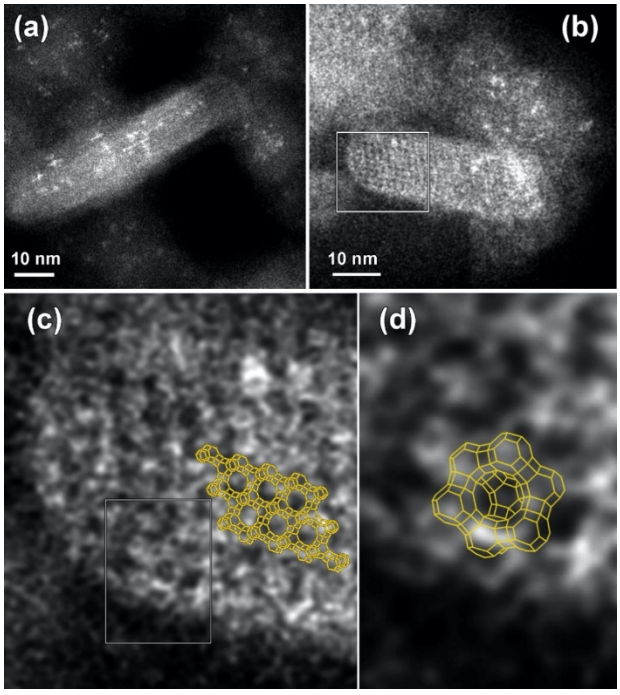

Fig. 3. HAADF-STEM analysis of the ZX-Bi sample: Low magnification HAADF-STEM images of different ZX-Bi nanoparticles viewed along two most informative directions: (a) $[112]_{FAU}$ and (b) $[011]_{FAU}$ zone axis; (c) and (d) correspond to the enlargement of the white boxes selected zones in figure (b)

and (c), respectively, overlaid with the corresponding structural model. The images reveal different Bi filling levels mainly in sodalite cage and 6MR prism: from high (white contrast) to almost empty (dark contrast).

Considering the ionic radius, it is reasonable to presume that Bi^{2+} and Bi^{3+} ions could occupy the sodalite cage and the hexagonal prism of the FAUX, respectively. However, the XPS results of Ag@ZX-Bi reveals the presence of Bi^{5+} with two characteristic peaks at 160.1 and 166.2 eV (Figure 4b)[29,30]. This result indicates that a redox reaction occurs between the Bi^{2+}/B^{3+} and Ag^{+}. It is important to mention that similar result was obtained in the absence of ethanol (used as an electron donor in case of Ag@ZX-V; Figure S7). Also, similar results was recorded after 30 days in dark (with lower absorbance intensity), showing a different process of silver reduction in comparison with Ag@ZX-V (Figure S8). Hence, a photo-assisted redox process between Bi^{2+}/Bi^{3+} and Ag^{+} is the most credible explanation supported by the selective detection of Bi^{5+}on Ag@ZX-Bi samples.

Fig. 5 shows the time progression of the Ag@ZX-Bi UV-visible spectrum versus the UV-irradiation time. A distinctive color change from milky white to magenta can be clearly observed (Insert **Figure 5**). The absorbance band positions indicate the presence of isolated Ag-CLs ($Ag_n^{\delta+}$) with different nuclearities (≠n) inside FAUX. These Ag-CLs have a characteristic absorbance in the UV region, similar to that observed previously for Ag@ZX-V samples (Figure S8; Table S3). The broad absorption extended over the 266-310 nm region, is usually assigned to the electronic transitions of few-atoms containing silver ionic clusters ($Ag_n^{\delta+}$), e.g., Ag_3^{+}, Ag_4^{2+}, ionic $Ag_8^{\delta+}$ [31,32]. The shoulders around 295 and 360 nm are characteristic fingerprints of hydrated Ag_4^{2+}.[33] A distorted symmetry due to the interaction with water molecules explains the Ag_4^{2+} absorption spectrum splitting with maximums at 295 and 360 nm[34]. A similar effect is most probably the origin of broad peak at 360 nm[35]. The super-atom orbitals model suggests that the Ag_4^{2+}electronic transitions are S-P transitions resulting from the contribution of 5S-based orbitals, i.e., from a doubly symmetric occupied orbital (S-Orbital) to an unoccupied orbital (P-orbital)[36]. The well-defined peak at 320 nm is usually assigned to the presence of the atomic Ag_8^{0} in the sodalite cage[37]. Each of the eight silver atoms is pointing toward one six-membered ring, thus forming a distorted cube inside the sodalite cages. The band at 380 nm is close to the characteristic absorption bands of silver species containing approximately seven nuclei embedded in zeolite cages[38,39]. It should be noted that the band's intensities reflect the abundance of the different $Ag_n^{\delta+}$ species (with n>δ), which can have different extinction coefficients.

Comparing to the metallic silver, the XPS analysis of Ag@ZX-Bi shows a shift to the higher bending energy (Figure S9-B), confirming the clusters/nanoparticles nature of the Ag particles.[40] The auger spectra (Figure S9-C) show two broad bands with kinetic energy near 349 nm and 354 nm with a shift of ≈2 eV compared to metallic silver. This demonstrates the ionic state of silver clusters.[41,42] This result is also confirmed by the IR analysis, using CO as probe molecule, which demonstrates the presence of both metallic and ionic silvers (Figure S10). Therefore, based on these results and the TEM data we conclude that silver particles are in form of reduced $Ag_n^{\delta+}$ clusters with a partial cationic charge (n>δ). Contrariwise to the UV region, Ag@ZX-Bi illustrates a very distinctive optical behavior in the visible range than that usually observed for the classical Ag-CLs and/or plasmonic Ag-NPs confined/supported in/on the zeolite. Interestingly, the spectra of Ag@ZX-Bi sample shows new bands at around 460, 502 and 535, 600 and 675 nm, which might be the origin of the magenta color. The shallow pink color has been previously reported on Bi-doped FAU zeolite after intense thermal treatments and the absorbance intensity is generally proportional to the Bi^{+} concentration[43]. Bi^{+} was characterized with two significant NIR-absorption bands at 500 and 700 nm and promoted by the thermal reduction of Bi^{3+}. However, no Bi^{+} in Ag@ZX-Bi is detected, as reveals the XPS characterization of the sample and reported previously (**Fig. 3**). Therefore, we conclude that the appearance of these new bands in the visible region, results from a strong interaction of the zeolite ligand and the reduced silver clusters by a transitional charge transfer (CT) and/or to a strong connection between the silver clusters through the zeolite channels[32]. Similar optical features were observed for the brick-red samples prepared upon dehydration of Ag containing zeolites A[31,34,44]. It is important to note that the UV-visible band positions are not affected by the nature of the sample (powder or suspension). However, the bands' relative intensity is dramatically modified, showing a solvatochrome effect of the liquid water (Figure S11-A). We should also mention that the Ag@ZX-Bi sample, compared to Ag@ZX-V, is very stable. The analysis repeated eight months after the preparation, for both suspension and powder forms, showed no significant alteration in their UV-visible spectra and crystallinity (Figure S11-B). To the best of our knowledge, such an exceptional optical stability is not reported for silver species (clusters or nanoparticles) up to date.

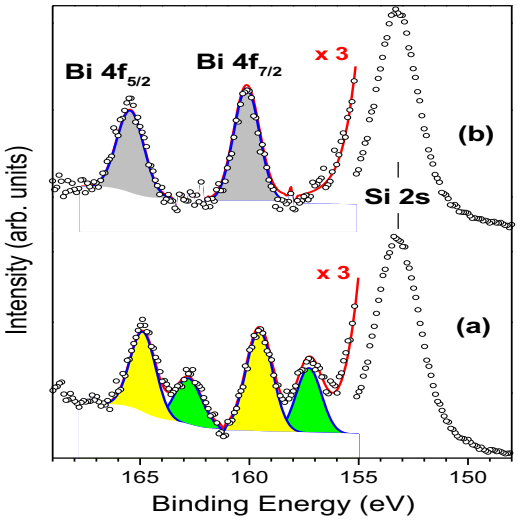

Fig. 4. Gaussian deconvolutions of the XPS spectra of ZX-Bi-3 (a) and Ag@ZX-Bi-3 (b) samples. The red lines correspond to the intensity sum of the different peak contributions.

A set of experiments was performed to better understand the Ag@ZX-Bi-3 sample behavior. First, the role of Bi^{n+} was investigated to highlight the characteristic of Ag@ZX-Bi. For this purpose, suspensions containing ZX, ZX-Bi-0.5, ZX-Bi-1.5 and ZX-Bi-3 were exposed to UV irradiation for 15 min in the presence of equimolar amounts of silver nitrate (Figure S12). No significant absorbance is observed for the pure zeolite showing the absence of any silver clusters. The UV-visible spectra Ag@ZX-Bi-3 and Ag@ZX-Bi-1.5 exhibit two mains narrow bands at 318 and 408 nm and differ from the ZX-Bi-0.5 spectrum (Figure S12). The 318 and 408 nm bands intensities are lower in case of Ag@ZX-Bi-1.5 with the appearance of the characteristic bands in the visible region, which is much more pronounced for Ag@ZX-Bi-3. On the other hand, zeolites prepared under similar conditions but at different crystallization times ($t_{cristal}$) are used to prepare a series of Ag-CLs-containing ZX-Bi-3 samples. The ICP analysis proves that the Bi content and Si/Al ratio is similar for all samples (Table S4). As shown in Figure S13, the increase of the FAUX samples' crystallinity ($t_{cristal}$<10h) impacts the abundance of the Ag-CLs but without a significant effect on their nature. However, when sodalite is the major phase (Figure S4g, $t_{cristal}$=48h), the optical behavior of the sample is dramatically changed. Therefore, there is a direct relationship between the zeolite framework morphology and the optical behavior of Ag@ZX-Bi-3 samples. The undirect contribution of Bi cations on the Ag@ZX-Bi optical behavior can't be totally excluded. However, the variation of the optical behavior (and not only on the absorbance bands' intensities) with the Bismuth concentration allows to exclude an important impact of the bismuth. E.g. if the Bi is impacting the optical behaviour, the variation of its concentration would affect the intensity instead of the band positions (wavelength). This conclusion is fully supported by the simulation of the cluster absorbance. Connecting the silver via the prismatic cages shifts the absorbance bands from near visible to the red region. The effect of the zeolite topology is also clear. The optical behavior changes between the FAU type and Sodalite type frameworks. On the other hand, it is still clear that the optical behavior of Ag@ZX-Bi sample depends on the specific topology of the faujasite structure. Namely, the FAU supercages are connected through double six-member rings forming hexagonal prisms. This structural unit is absent in the sodalite structure. In Ag@ZX-Bi, Ag^{+} has a strong affinity for the site I and I' that are located in the hexagonal prism faces between the sodalite cages[13], while Bi^{n+} occupies mainly the sodalite cages. The positioning of Ag in the 6MR prism, in addition to the abundance of the Bi cations in the sodalite cages, contributes to the formation of Ag clusters and thus ensures the interconnection between silver clusters. This connection does not exist in the sodalite structure and consequently, the silver clusters remain isolated. On the other hand, the relatively low concentration of Bi active sites in FAUX leads solely to the formation of isolated Ag-CLs. Therefore, the increasing of the Bi^{3+}/Bi^{2+} active sites concentration might promote the connectivity of the Ag-CLs and the formation of quasi-AgNPs. This is due to the increase of the reduced silver concentration reducing then their inter-distance.

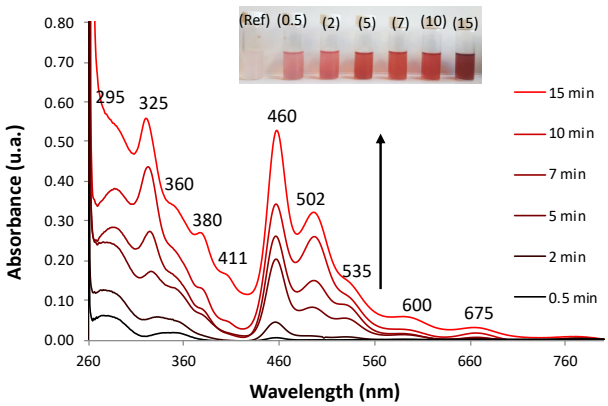

Fig.5. Time evolution of UV-vis absorption spectra of ZX-Bi suspensions after (a) 0,5, (b) 2, (c) 5 (d) 7, (e) 10 et (f) 15 min of UV irradiation in presence of 10^{-2} M of $AgNO_3$. (Ref) correspond to the sample before irradiation. Conditions: lamp Hg-Xe; polychromatic = 205 mW/cm^2; filter cut infrared; total volume = 5 ml; [ZX-Bi] = 2.4 g/l. Inset: images of the corresponding suspensions.

The continuous wave (CW) photoluminescence (PL) measurements shed more light on the optical behavior of the Ag@ZX-Bi-x samples (x= 0.5, 1.5 and 3). The measurements were carried out at room temperature using two excitation lasers at 266 nm and 488 nm. For excitation at 266 nm, we observe several PL bands, depending on the Bi content. The most intense band position is at 2.06eV (600 nm). The less intense bands are observed respectively at 2.22eV (558 nm) and at 2.35eV (527nm). Upon excitation at 488 nm, new PL bands at 2.67eV (464 nm) and at 1.39eV (892 nm) are observed with very low intensity; the later are attributed to the high Bi content (Fig. 6 a and b). The bands observed in all spectra, 2.06eV (600nm), 2.22eV (558 nm) and 2.35eV (527 nm), seem independent of the type active center or its concentration (Figure S14). We attribute these bands to isolated silver clusters in the sodalite cages. For example, the emission bands observed at 527 and 558 nm are similar to the ones associated with the trinuclear and tetranuclear silver species[13,45]. These assignments agree with the UV-visible absorbance analysis of the samples, which indicates the presence of common Ag species with characteristic UV absorbance and new species with characteristic visible absorbance for Ag@ZX-Bi samples with relatively high Bi content. This latter seems have very low (or no) radiative emission in the visible range (characteristic behavior of plasmonic particles).

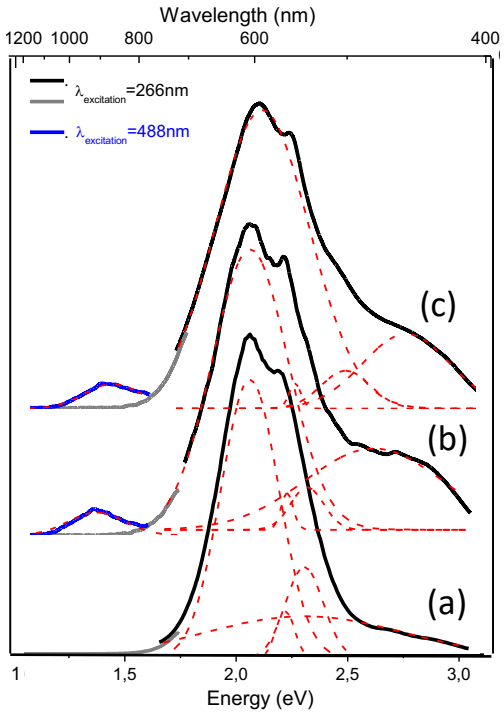

Fig. 6. PL spectra of (a) Ag@ZX-Bi-0.5, (b) Ag@ZX-Bi-1.5 and (c) Ag@ZX-Bi-3.0 samples. The excitation laser wavelength is either 266 nm (black&grey) or at 488 nm (blue). PL bands were fitted using the Gaussian function (doted red lines). Long pass filters were used with cut-on wavelength at 700 nm for grey and blue curves.

This assignment was further supported by the TEM results. Figure 7 shows high-resolution TEM images along the most informative [011] FAU zone axis. The morphology of ZX nanoparticles remains intact with clearly expressed faceting with <111> planes. Ag clusters appear as dark spots in the TEM images (**Fig. 7a-b**) and as bright white dots (Z=47) in the HAADF-STEM images (**Fig. 7c-e**), where the contrast is proportional to atomic number (~Z^2) and thickness.

In the latter, the dark spots correspond to the supper cages and/or surrounding ZX framework, which is not clearly resolved due to the low sum HAADF-STEM contrast of silica-alumina zeolite framework (Z_{Si}=14; Z_{Al}=13, Z_O=8) and large difference with the atomic number of Ag. Despite the high sensitivity of the Ag@ZX-Bi particles to the electron beam and tendency to agglomerate in larger silver NPs, it was possible to acquire high-resolution image along the [011] and [112] zone axis of Ag@ZX-Bi crystallite in both mode - HRTEM (**Fig. 7b**) and HAADF-STEM (**Fig. 7e**) - using low doses and weak e-beam conditions. Thus, the lattice planes of Ag clusters were resolved. The corresponding Fourier Transform (FT) patterns (insert **Fig. 7b**) confirm the presence and the 3D arrangement of Ag [111] particles within the pores of FAU-type structure.

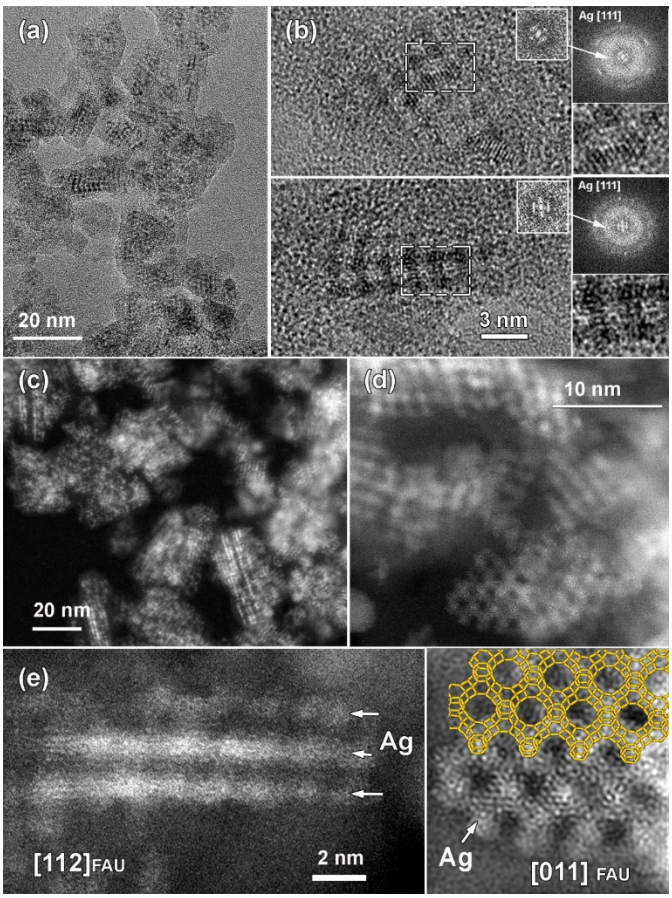

Fig. 7. TEM analysis of the Ag@ZX-Bi sample: (a) bright-field low magnification TEM images of Ag@ZX-Bi; (b) HRTEM image of single Ag@ZX-Bi crystallites revealing resolved Ag lattice planes following the FAU structure. The corresponding FT pattern confirmed the structure and the 3D arrangement of the Ag clusters aligned to the FAU framework (see enlargements of the central FT spots). (c) Low magnification HAADF-STEM image of Ag@ZX-Bi. Bright contrast Ag nanostructures are clearly visible. (d) High-resolution HAADF-STEM image of Ag@ZX-Bi. (e) High resolution HAADF-STEM images of Ag@ZX-Bi structures close to [112] (left panel) and to [011] (right panel) FAU zone axis. Ag nanostructures within ZX-Bi structure exhibiting bright contrast are marked with white arrows. The structural model of FAU is overlaid on the experimental image.

The Ag sub-nanoparticles appear in projection to have close to the ball shape with a typical diameter of about 1.0 nm, interconnected by Ag “nanobridges” and forming checker board pattern reflecting the [011] FAU structure symmetry. The size of Ag is compatible with the the 6-member ring prism of FAU structure. The Ag in such position makes a nanobridge between the silver clusters situated in the sodalite cage, as shown in **Fig. 7e** (insert). The [011] FAU skillet structural model is placed over the experimental [011] HAADF-STEM image (**Fig. 7e)**. The HAADF-STEM image of Ag@ZX-Bi projected on [112] zone axis reveals the presence of silver nanoparticle situated in the sodalite cages connected through the 6MR prism thus creating a 3D nanostructure. The needles-like silver particles (Figure 7e) are more pronounced and longer than those observed in our previous work on Ag@-ZX-V. This could explain the characteristic visible absorbance of the silver quasi-nanoparticles. It should be noted that

due to the low concentration of the Bi, we assume that the white spot corresponds mainly to the silver particles which are clearly much more abundant than Bi (Fig. 3). Taking into account the redox process, the oxidation of Bi^{2+}, Bi^{3+} to Bi^{5+} generate three to two reduced silver, respectively. This reduced silver atoms are surrounded with cationic silver atoms to form the clusters making silver much more abundant than bismuth. The oxidation of the Bi allows recompensate the positive charge of reduced silver. The IR spectra of Ag@ZX-Bi (Fig. S17) (1600-1300 cm^{-1}) reveal the presence of residual nitrate indicating that the excess of the positive charge of bismuth (in respect to the zeolite framework) is recompensated by the negative charge of nitrate as counter ion.

MNPBEM modeling experiments (please see the SI for more details) were performed to understand better the optical behavior of nanostructured silver species in the Faujasite (Ag-FAU-Rep) pore space (Figure 8A). We have modelled the far-field response in terms of extinction absorption and scattering cross-section spectra and near field responses in terms of field enhancement map (Figure 8B). The extinction, absorption, and scattering cross-sections spectra of isolated and interconnected Ag-FAU nanoparticles with two perpendicular excitation polarizations (E//xO; E//yO) were calculated. The extinction cross-section sums of the absorption were found clearly greater than the scattering one. A plasmon narrow extinction band centered at 384 nm, independent of excitation polarization, is observed in the samples with isolated silver nanostructures in the sodalite cages (i.e., Ag-free 6MR prism). This band is similar to that observed for a single Ag cluster (Figure S15) and experimentally observed in the case of Ag@ZX-V and Ag-ZX-Bi-0.5 (ZX-Bi with low Bi content). However, in the case of Ag-FAU nanostructures with interconnected silver clusters (Ag in the sodalite cage and 6MR prism), the extinction spectra show new extinction bands distributed in the visible region (370-700nm).

The simplification of the modelled system is probably the reason for the difference in the band's positions between the simulated and the experimental spectra (more details in the experimental section). Nevertheless, it reveals important information concerning the nanostructure shape effect on the global optical behavior. More significantly, the results confirm the hypothesis that the interconnection of silver clusters through the zeolite channels is responsible for absorbing multiple bands in the visible range. The simulation shows that with the exception of 384 nm and 370 nm bands the intensity depends on the polarization angle (Figure S16). This evidence that those resonances arise on structures with less symmetry than the individual particle in the sodalite cage or the 6MR prism and that they might be due to delocalized mode over several of those elements. The origin of different bands obtained on single silver faujasite nanostructures were investigated by exploring the plasmon response of elemental building blocks. Large and small individual nanoparticles were considered: rods formed by two large and a small nanoparticle (vertical and oriented at 19.47°/xOy plan); faujasite's basis ring formed by six rods; conical top structure formed by three rods oriented at θ=120° (Figure S16). The plasmon response in term of extinction cross-section spectrum of those building blocks was calculated and compared to one of silver faujasite nanostructures. This comparison allowed us to confirm that the resonance centered at 383 nm is due to the individual/isolated response of large and small silver nanoparticles/clusters reported above or to rods parallel to wavevector (perpendicular to xOy plane). The resonances between 386 and 500 nm can be attributed to resonances occurring in rods oriented out of the perpendicular axis to xOy plane. Resonances occurring above 500 nm are attributed to resonance occurring in the whole ring and conical top structures (**Fig. 8B**). Larger structures created by adding several faujasite unit cells resulting in the linear chain were investigated, leading to comparable cross-section spectra (Figure 8) with resonance peaks ranging from 383 to 700 nm.

The calculated near-field enhancement maps for isolated and interconnected silver nanostructures with resonance energy at 370, 383 and 549 nm are reported in **Fig. 8B**. Localized resonance around each constituting nanoparticle was found on isolated silver Faujasite nanostructures, while delocalized resonance over several constituting nanoparticles was found on interconnected silver Faujasite nanostructures. This result confirms the existence of delocalized plasmon modes on several Ag-FAU building blocks leading to numerous extinction bands whose positions are red-shifted up to 700 nm. The near field enhancement map at 549 nm evidences that the red-shifted plasmon resonance occurs in a single-cell nanostructure. Considering that the plasmon decay follows three different channel processes with Drude friction-like dissipation, inter-band transitions, and generation of energetic hot electrons[46], we may have a different kind of behavior depending on the spectral position of excitation. For short wavelengths (high energy), we may have energy transfer to resonant energy levels of luminescent species, leading to enhanced photoluminescence (as observed above under 266 nm of excitation). For larger wavelengths (lower energy), only the dissipation process may occur with Drude friction or electron-phonon interactions leading to heat release in the local nanostructure environment.

ARTICLE

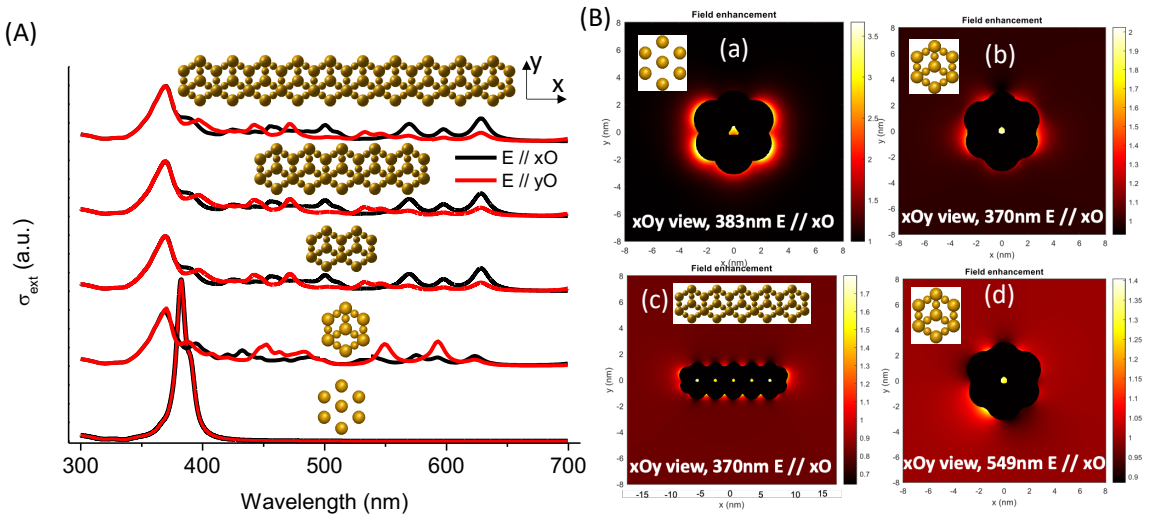

Fig. 8. (A) Extinction cross-section of silver nanostructures with isolated and interconnected nanoparticles in a single unit cell, two interconnected unit cells, five interconnected unit cells, and ten interconnected unit cells with polarization along xO and yO axis. (B) Near-field enhancement maps for isolated silver (a) and interconnected (b,d) silver-replica nanostructures resonance energy of one (b) and five (c) unit cells at 370 nm (b,c), 383 nm (a), and 549 nm (d).

The operando IR analysis have been used to elucidate the plasmonic behavior of the Ag@ZX-Bi-3 sample. Under visible light irradiation, it shows an immediate response with fast water desorption for almost 80 % in the first three minutes of irradiation (**Fig. 9A**).

This loss is usually taking place at around 200°C (**Fig. 9B)**, and in agreement with the TG result for ZX-Bi (**Fig. 3B**)). It is important to mention that this effect is more than two times higher than that observed with Ag@ZX-V (Figure S17) and that there are no responses for Ag@ZX-Bi and Ag^{+}@ZX-Bi under monochromatic UV (366 nm) or visible (>390 nm) light irradiations, respectively. Therefore, this attitude is directly related to the presence of the Ag-quasi-NPs (Ag-QNPS). Another noteworthy behavior is observed on the activated samples (after 30 min of visible irradiation at 28°C). The IR spectrum of this sample shows a reversible and instantaneous shift toward the lower wavenumbers (for 3.4 cm^{-1}) in the vibration region of ν(OH) under visible irradiation in respect to that collected in dark (Figure 9C-D). Such an effect is usually a sign of a temperature increase for few hundreds of degrees[47].

The relationship between the ν(OH) band and the temperature was measured on Ag@ZX-Bi series of samples (Figure S18). The results show that the shift of 3.4 cm^{-1} corresponds to a heating temperature of 190°C. Under permanent visible irradiation and with the increase of the sample temperature, the variation of ν(OH) (Figure S18-A) is almost constant ($\Delta\nu$(OH~3.5 cm^{-1}) until 150°C. However, the shift is similar (in dark or under visible light) for a temperature equal or higher than 200°C. The HRTEM analysis shows that the activation of Ag@ZX-Bi at T≥200°C promotes the formation of external AgNPs (Figure S19), probably due to the migration and aggregation of the silver on the zeolite surface. This explains the major drop of the plasmonic behavior of the S-QNPs. It should be noted that the zeolite surface is rich in OH groups, but without direct contact with the Ag-QNPs. The instantaneous effect on these sites' vibration frequencies allows thinking that the energy transfer from the Ag-QNPs to the OH is probably radiative and agrees with the water desorption observed during the irradiation of Ag@ZX-Bi under visible light.

ARTICLE

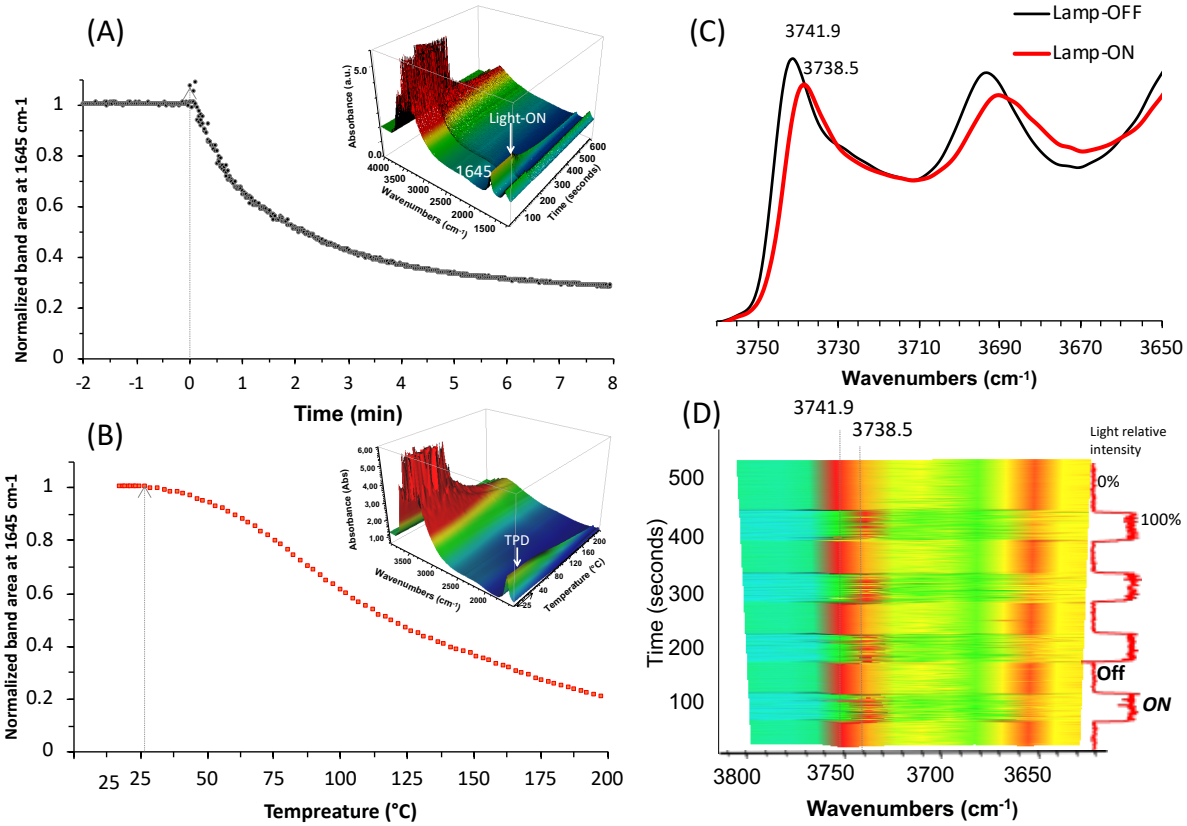

Fig. 9. Evolution of the IR band area (centered at 1645 cm^{-1}) of the adsorbed water on the as-prepared Ag@ZX-Bi-3 samples versus (A) the visible light irradiation time at 25°C, and (B) the temperature in dark. Inset: 3D mapping of the corresponding original spectra. The arrow corresponds to the turn on the light (t=0s) and the starting point heating (rate = 1.75°C/min), respectively. Experiment conditions: Ar flow (25 cm^3/min); m_{cat}=20 mg (pellet with 2 cm^2 of diameter and 65 µm of thickness; Light source used in (A) Xe lamp with cut UV filter (l>390 nm) and irradiance of ≈ 150 mW/cm^2. (C) IR spectra of Ag@ZX-Bi sample in the vibration region of the SiOH in dark (black; lamp-OFF) and under visible irradiation (red; Lamp-ON). Sample activated at 28°C under visible light for 30 min. (D) 2D mapping of the band intensity variation in the 3800-3650 cm^{-1} region at different cycles of lamp-OFF/lamp-ON (red and blue-green correspond to the higher and lower intensity, respectively). (light relative intensities (0% or 100%): low position: shutter close; high position: shutter open). The vertical scale axis corresponds to the time of the experiments. Note: (C) and (D) were measured on the same sample pellet and under the same conditions used in (A).

4 Conclusion

Bismuth (Bi^{2+}/Bi^{3+}) doped zeolite nanoparticles (ZX-Bi), successfully prepared by one-pot hydrothermal synthesis and stabilized as colloidal suspensions, were used for the preparation of bridged silver clusters. The UV-irradiation of the ZX-Bi suspensions in the presence of silver nitrate promotes the formation of reduced silver particles (Ag@ZX-Bi) in the zeolite micropore space. The set of experimental results revealed that the optical behavior of the confined silver particles depends on the Bi concentration initially introduced in the zeolite. The composite sample's UV-visible absorbance shows narrow bands in the visible range (400-800 nm), characteristic of metal nanoparticles with well-defined sizes. The TEM analysis, the photoluminescence results, and the boundary element method (BEM) approach showed that the Ag's unique optical behavior is a consequence of the formation of interconnected silver clusters (silver quasi-nanoparticles) through the zeolite channels. The IR operando analysis of the samples in dark and under visible light confirmed the surprising plasmonic behavior of the Ag@ZX-Bi samples and registered local heating equivalent to 190°C under visible irradiation, a characteristic behavior of plasmonic nanoparticles. Therefore, to our knowledge, the gap between clusters and plasmonic nanoparticles with well-controlled and reproducible size of Ag-QNPs is bridged for the first time. The

simplicity of the used method allows an easy scaling-up for different possible applications (μ-sensors, electronic, optic, etc.).

Author Contributions

The manuscript was prepared written through the contributions of all authors. All authors have approved the final version of the manuscript.

Conflicts of interest

The authors declare that no competing interest.

Acknowledgements

F. Douma and M. El-Roz acknowledge the PHC Tassili program (17MDU983) and European Regional Development Fund (ERDF), Normandy region (RAPHYD project), for the financial support. Authors acknowledges the colleagues' Mama Lafjah, Fatiha Djafri and Jaun Pablo Bolletta for the scientific discussions and supports.

Notes and references

[1] Y. Lu, W. Chen, *Chemical Society Reviews*, 2012, **41**, 3594-3623.
[2] I. Chakraborty, T. Pradeep, *Chemical reviews*, 2017, **117**, 8208-8271.
[3] T. Q. Yang, B. Peng, B. Q. Shan, Y. X. Zong, J. G. Jiang, P. Wu, K. Zhang, *Nanomaterials*, 2020, **10(2)**, 261.
[4] N. Sakai, S. Nakamura, T. Tatsuma, *Dalton Transactions*, 2013, **42**, 16162-16165.
[5] A. Royon, K. Bourhis, M. Bellec, G. Papon, B. Bousquet, Y. Deshayes, L. Canioni, *Advanced materials,* 2010, **22**, 5282-5286.
[6] Y. Wang, C. Dai, X. P. Yan, *Chemical Communications*, 2014, **50(92)**, 14341-14344.
[7] Y. Yu, J. Geng, E. Y. X. Ong, V. Chellappan, Y. N. Tan, *Advanced healthcare materials*, 2016, **5**, 2528-2535.
[8] J. Li, Y. Dai, S. Wang, C. Han, K. Xu, *Sensors and Actuators B: Chemical*, 2016, **232**, 1-8.
[9] L. Shang, S. Dong, *Biosensors and Bioelectronics*, 2009, **24**, 1569-1573.
[10] I. Díez, M. Pusa, S. Kulmala, H. Jiang, A. Walther, A. S. Goldmann, R. H. Ras, *Angewandte Chemie International Edition*, 2009, **48**, 2122-2125.
[11] M. Cao, R. Pang, Q. Y. Wang, Z. Han, Z. Y. Wang, X. Y. Dong, T. C. Mak, *Journal of the American Chemical Society*, 2019, **141**, 14505-14509.
[12] T. Wu, D. Yin, X. Hu, B. Yang, H. Liu, Y. P. Xie, G. G. Gao, *Nanoscale*. 2019, **11(35)**, 16293-16298.
[13] T. Altantzis, E. Coutino-Gonzalez, W. Baekelant, G. T. Martinez, A. M. Abakumov, G. V. Tendeloo, J. Hofkens, *ACS nano*, 2016, **10**, 7604-7611.
[14] D. Yao, S. Xu, Y. Wang, H. Li, *Materials Chemistry Frontiers*, 2019, **3**, 1080-1084.
[15] S. Aghakhani, D. Grandjean, W. Baekelant, E. Coutiño-Gonzalez, E. Fron, K. Kvashnina, P. Lievens, *Nanoscale*, 2018, **10**, 11467-11476.
[16] T. Yumura, A. Oda, H. Torigoe, A. Itadani, Y. Kuroda, T. Wakasugi, H. Kobayashi, *The Journal of Physical Chemistry C*, 2014, **118**, 23874-23887.
[17] a) M. El-Roz, I. Telegeiev, N. E. Mordvinova, O. I. Lebedev, N. Barrier, A. Behilil, V. Valtchev, *ACS applied materials & interfaces*, 2018, **10(34)**, 28702-28708.
b) H. I. Hamoud, M. Lafjah, F. Douma, O. I. Lebedev, F. Djafri, V. Valchev, M. El-Roz, *Solar Energy*, 2019, **189**, 244-253.
[18] M. El-Roz, L. Lakiss, I. Telegeiev, O. I. Lebedev, P. Bazin, A. Vicente, V. Valtchev, *ACS applied materials & interfaces*, 2017, **9**, 17846-17855.
[19] F. G. De Abajo, A. Howie, *Physical Review B*, 2002, **65**, 115418.
[20] U. Hohenester, A. Trügler, *Computer Physics Communications*, 2012, **183**, 370-381.
[21] P. B. Johnson, R. W. Christy, *Physical review B*, 1972, **6**, 4370.
[22] A. M. Kuznetsov, M. S. Shapnik, A. N. Masliy, K. V. Zelenetskaya, *Russian journal of electrochemistry*, 2002, **38**, 669-675.
[23] H. Awala, J. P. Gilson, R. Retoux, P. Boullay, J. M. Goupil, V. Valtchev, S. Mintova, *Nature materials*, 2015, **14**, 447-451.
[24] X. Qin, Y. Li, D. Wu, Y. Wu, R. Chen, Z. Ma, J. Qiu, *RSC advances*, 2015, **5**, 101347-101352.
[25] A. Yousif, R. M. Jafer, S. Som, M. M. Duvenhage, E. Coetsee, H. C. Swart, *RSC Advances*, 2015, **5**, 54115-54122.
[26] H. Li, Z. Yang, J. Zhang, Y. Huang, H. Ji, Y. Tong, *Applied Surface Science*, 2017, **423**, 1188-1197.
[27] M. Majerová, R. Klement, A. Prnová, J. Kraxner, E. Bruneel, D. Galusek, *Royal Society open science*, 2018, **5**, 181667.
[28] H. T. Sun, Y. Matsushita, Y. Sakka, N. Shirahata, M. Tanaka, Y. Katsuya, K. Kobayashi, *Journal of the American Chemical Society*, 2012, **134**, 2918-2921.
[29] M. G. Sales, L. Herweyer, E. Opila, S. McDonnell, *Applied Surface Science*, 2020, **508**, 145256.
[30] C. Lv, G. Chen, X. Zhou, C. Zhang, Z. Wang, B. Zhao, D. Li, *ACS applied materials & interfaces*, 2017, **9**, 23748-23755.
[31] I. Tuzovskaya, N. Bogdanchikova, A. Pestryakov, V. Gurin, A. Simakov, & V. Lunin, *Advances in the Understanding and Application of Catalysts*, 2003, **248**.
[32] V. S. Gurin, N. E. Bogdanchikova, V. P. Petranovskii, *The Journal of Physical Chemistry B*, 2000, **104**, 12105-12110.
[33] T. Yumura, A. Oda, H. Torigoe, A. Itadani, Y. Kuroda, T. Wakasugi, H. Kobayashi, *The Journal of Physical Chemistry C*, 2014, **118**, 23874-23887.
[34] E. Fron, S. Aghakhani, W. Baekelant, D. Grandjean, E. Coutino-Gonzalez, M. Van der Auweraer, J. Hofkens, *The Journal of Physical Chemistry C*, 2019, **123**, 10630-10638.
[35] N. T. Cuong, H. M. T. Nguyen, M. P. Pham-Ho, M. T. Nguyen, *Physical Chemistry Chemical Physics*, 2016, **18**, 18128-18136.

[36] T. Yumura, M. Kumondai, Y. Kuroda, T. Wakasugi, H. Kobayashi, *RSC advances*, 2017, **7**, 4950-4959.
[37] B. Concepción-Rosabal, G. Rodríguez-Fuentes, N. Bogdanchikova, P. Bosch, M. Avalos, V. H. Lara, *Microporous and Mesoporous Materials*, 2005, **86**, 249-255.
[38] R. Kellerman, J. Texter, *The Journal of Chemical Physics*, 1979, **70**, 1562-1563.
[39] E. Gachard, J. Belloni, M. A. Subramanian, *Journal of Materials Chemistry*, 1996, **6**, 867-870.
[40] H. S. Shin, H. C. Choi, Y. Jung, S. B. Kim, H. J. Song, H. J. Shin, *Chemical physics letters*, 2004, **383**, 418-422.
[41] A. M. Fonseca, I. C. Neves, *Microporous and mesoporous materials*, 2013, **181**, 83-87.
[42] O. Fenwick, E. Coutiño-Gonzalez, F. Richard, S. Bonacchi, W. Baekelant, D. de Vos, P. Samorì, *Small,* 2020*,* **16**, 2002063.
[43] Z. Bai, M. Fujii, T. Hasegawa, K. Imakita, Y. Miwa, M. Mizuhata, S. Hayashi, *Microporous and mesoporous materials*, 2011, **145**, 21-25.
[44] R. Seifert, R. Rytz, G. Calzaferri, *The Journal of Physical Chemistry A*, 2000, **104(32)**, 7473-7483.
[45] B. Dong, R. Retoux, V. De Waele, S. G. Chiodo, T. Mineva, J. Cardin, & S. Mintova, *Microporous and Mesoporous* Materials, 2017, **244**, 74-82.
[46] L. V. Besteiro, X. T. Kong, Z. Wang, G. Hartland, A. O. Govorov, *Acs Photonics*, 2017, **4**, 2759-2781.
[47] V. Zholobenko, C. Freitas, M. Jendrlin, P. Bazin, A. Travert, & F. Thibault-Starzyk, *Journal of Catalysis*, 2020, **385**, 52-60.